Nugget Formation and Performance of Resistance-Rivet-Welded Al/Steel Joints

When RRW with solid rivets was used to join 6016 aluminum alloy and CR1180T ultra-high strength steel, three failure modes were identified

BY M. LI, R. SHI, S. YU, Z. GAO, T. SHI, S. AO, AND Y. LI

Abstract

Resistance rivet welding (RRW) is a method developed in recent years for the joining of dissimilar materials. In this study, RRW with solid rivets was used to join 6016 aluminum alloy and CR1180T ultra-high strength steel. The nugget formation process was investigated in terms of dynamic resistance, microstructure analysis, and microhardness measurement. The mechanical properties and failure mode of RRW joints were also investigated. The results showed that the Al under the rivet leg gradually melted from the middle to both sides during the piercing stage. Molten Al was squeezed into the space under the rivet cap. A mushroom-shaped weld nugget was first formed inside the steel sheet and gradually grew toward the rivet. The microstructure of the weld nugget was coarse martensite. A layer of uniform intermetallic compounds was formed between the rivet leg and the Al sheet. Three failure modes — interface failure, pull-out failure (PF), and Al sheet failure —were identified. The strain distribution of the joints with three failure modes in the tensile process was compared. Under the optimal parameters, the failure mode of the RRW joint was PF, and the average maximum tensile-shear force of the joints reached 11.4 kN.

Keywords

- Resistance Rivet Welding
- Solid Rivet
- Al/Steel
- Nugget Formation Process
- Joint Performance

https://doi.org/10.29391/2025.104.016

Introduction

In the automotive industry, reducing body weight is a critical strategy for energy saving and emission reduction. Due to its lightweight and high specific strength, aluminum alloy has garnered significant attention from the automotive sector (Refs. 1, 2). The integration of Al/steel hybrid structures harnesses the benefits of both materials, thereby enhancing energy conservation and reducing emissions while maintaining safety and reliability (Refs. 3–5). Resistance spot welding (RSW) stands out in automobile body manufacturing due to its ease of adaptability to automation, high efficiency, and cost-effectiveness (Refs. 6–8). When RSW is employed to join Al alloys and ultra-high strength steels (UHSSs), the significant differences in their metallurgical properties lead to the formation of intermetallic compounds (IMCs) at the joint, resulting in reduced joint performance (Refs. 9–11).

To mitigate IMC formation, researchers have developed thermomechanical hybrid joining processes. Meschut et al. (Ref. 12) introduced the resistance element welding (REW) process, which avoids IMC formation at the main load-bearing interface by incorporating holes in the Al sheet and auxiliary steel rivets. Ling et al. (Refs. 13, 14) investigated the properties of REW joints of 6061 Al alloy and uncoated 22MnMoB boron steel. Their findings demonstrated that REW joints exhibit higher tensile-shear strength and better toughness. Yang et al. (Refs. 15–17) studied the microstructure and mechanical properties of REW joints of DP780 steel and 6061 Al alloy. They identified two types of IMCs at the Al/steel interface: a tongue-like Fe_2Al_5 layer on the steel side and a finger-like Fe_4Al_{13} layer on the Al alloy side. Notably, dislocations were observed at the Fe_2Al_5 grain boundaries for the first time. At the same time, nano twins and stacking faults were detected in the Fe_4Al_{13} grains, indicating that planar defects primarily resulted from rapid cooling.

The REW process requires a punching operation before welding, which reduces efficiency and increases cost. To

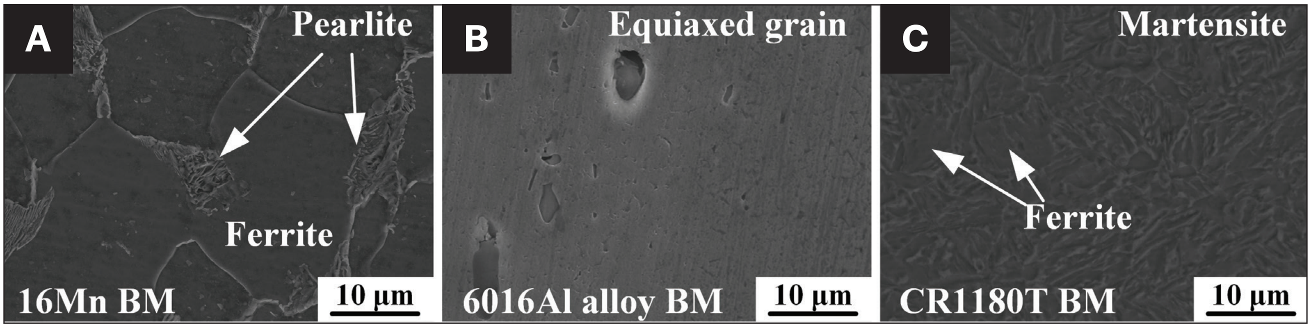

Fig. 1 — Microstructure of base materials: A — 16Mn; B — 6016 Al; C — CR1180T.

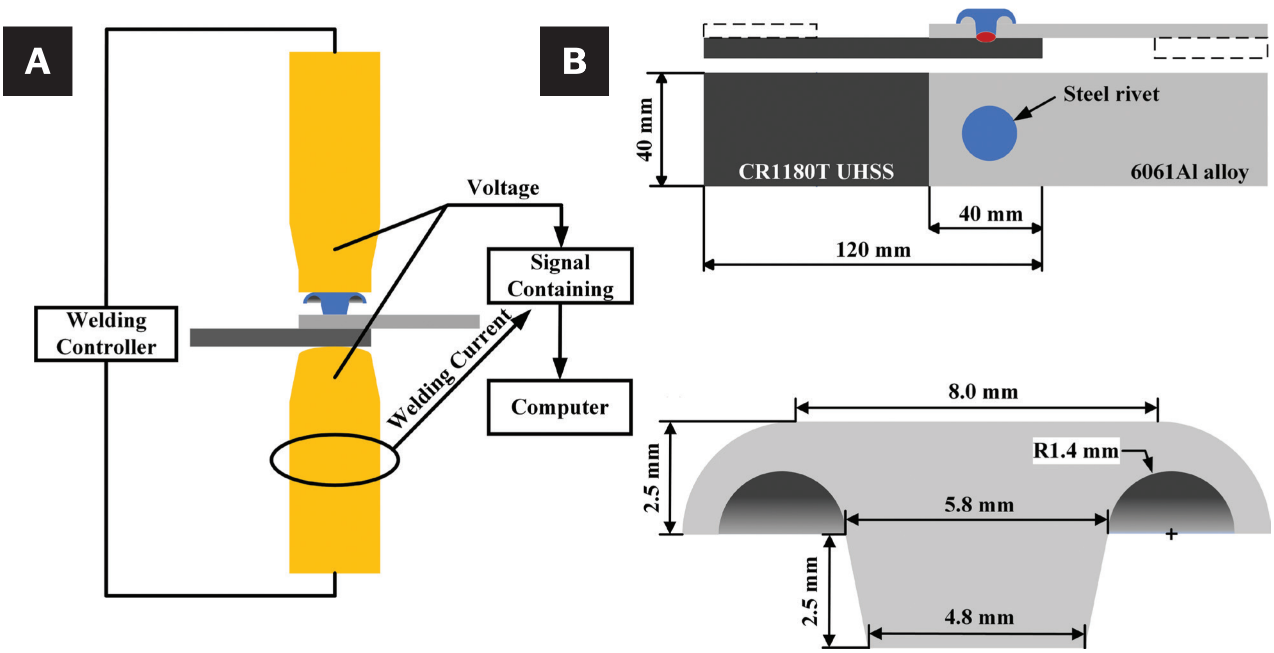

Fig. 2 — Schematic diagram of the: A — Signal collecting system; B — tensile-shear test; C — rivet structure and size.

Table 1 — Chemical Composition of Materials

Materials	C	Si	Mn	P	S	V	Ni	Ti	Fe	Al	Zn	Cr	Mg
16Mn	0.2	0.55	1	0.04	0.04	0.02	0.015	0.02	Bal.	—	—	—	—
6016 Al	—	1.33	0.04	—	—	—	—	0.06	0.1	Bal.	0.06	0.2	0.6
CR1180T	0.23	0.5	3	0.04	0.015	—	—	—	Bal.	—	—	—	—

further simplify the REW process, Hou et al. (Ref. 18) devised an integrated joining technique of punch-riveting and spot welding, facilitating rapid and reliable joining across various materials. Niu et al. (Ref. 19) named this method resistance rivet welding (RRW). Current research on RRW primarily focuses on using semi-hollow rivets and taper rivets (a kind of solid rivet). For example, Niu et al. investigated the RRW process using semi-hollow rivets and successfully achieved reliable joining between Al alloys and steel (Refs. 19, 20), Mg alloys and steel (Ref. 21), and Al alloys and Ti alloys (Ref. 22). The results indicated that RRW with semi-hollow rivets could effectively join dissimilar metals, with the joints mainly consisting of a mixed fusion zone (FZ) containing IMCs. Niu et al. (Ref. 23) also used RRW with taper rivets to join Al alloys

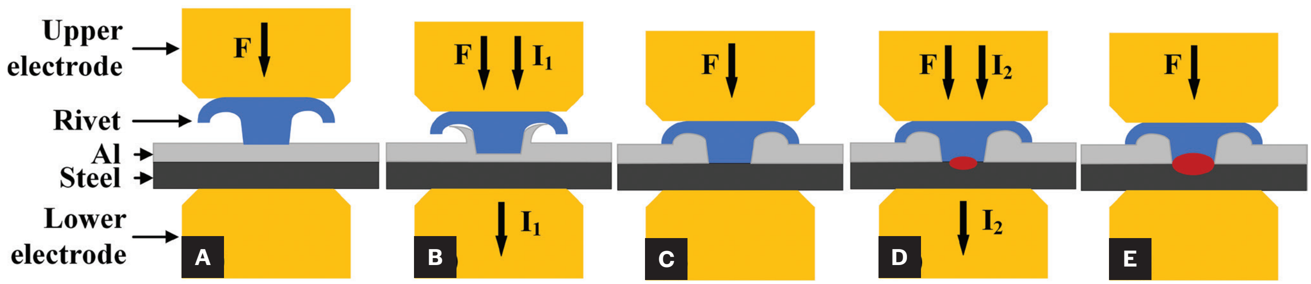

Fig. 3 — Schematic diagram of the RRW process: A — Positioning stage; B — piercing stage; C — cooling stage; D — welding stage; E — holding stage.

Table 2 — Mechanical Properties of Materials

Materials	Tensile Strength/MPa	Yield Strength/MPa	Elongation/%
16Mn	470	345	7.5
6016 Al	315	205	15
CR1180T	1180	850	6

and press-hardened steel. Unlike the semi-hollow rivet, the FZ structure of these joints was martensitic. Fei et al. (Refs. 24, 25) studied RRW process parameters with taper rivets and the effect of adding interlayers on joint performance. They found that total heat input and heat input per unit time were the main factors affecting joint performance. The addition of an interlayer was found to moderately enhance the tensile strength of the joints, although some IMCs were still present at the interface. Lou et al. (Ref. 26) investigated the effect of aging time (175°C for 35, 180, and 360 min) on the microstructure and mechanical performance of the whole resistance-rivet-welded (RRWed) Al/St joints. The results showed that the maximum peak load of the interfacial fracture and button pullout fracture joints increased by 13% and 26% with the extension of post-heat treatment time, respectively.

Neither semi-hollow nor taper rivet RRW joints can avoid IMCs at the main load-bearing interface, resulting in suboptimal mechanical properties. In the authors' previous work (Ref. 27), a solid rivet was designed, and the effect of rivet dimensions on the joint performance of RRWed aluminum alloy to ultra-high strength steel was investigated. This study employed solid rivets with optimized dimensions to conduct RRW of aluminum alloy to UHSS. The macromorphology, microstructure, dynamic resistance, and mechanical properties of RRW joints were investigated to better understand the RRW with solid rivets.

Experimental Procedure

Materials

The materials used in this study included 1.5 mm-thick 6016-T6 Al alloy, 2.0 mm-thick CR1180T ultra-high strength steel, and solid rivets made of 16Mn steel. The width and length of all sheets were 40 mm × 120 mm. These materials' chemical compositions and mechanical properties are listed in Tables 1 and 2. The microstructures of three base materials (BMs) are shown in Fig. 1. 16Mn steel is composed of ferrite and pearlite, 6016 Al alloy is composed of fine equiaxed grains, and CR1180T UHSS is a dual-phase steel composed of martensite and ferrite.

RRW Process

Before welding, the oxide layers on the 6016 Al alloy surfaces were removed with SiC paper, then the surface of all specimens was cleaned with alcohol. The RRW process was conducted on a WDB-400 intermediate frequency inverter resistance welding machine. A self-designed fixture was used to position the rivet before welding. The upper electrode was a flat electrode with a diameter of 13 mm, and the lower electrode was a spherical electrode with a spherical radius of 100 mm. The welding electrodes were cooled by water during welding. The voltage and current during the RRW process were measured by an external signal collector with a time interval of 1 ms, as shown in Fig. 2A. All the experiments were conducted in a lap-shear configuration, where the 6016 Al alloy was placed on the top of the CR1180T UHSS, as shown in Fig. 2B. The rivet structure and size are shown in Fig. 2C. The determination of the rivet size was based on our preliminary study (Ref. 27). The welding

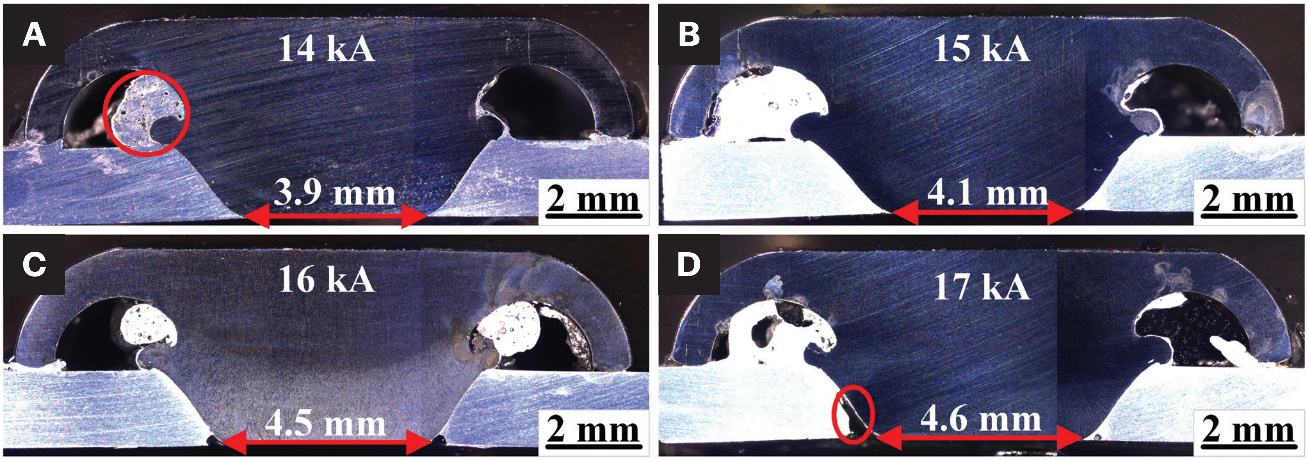

Fig. 4 — Macroscopic morphologies of the joints made with piercing currents of: A — 14 kA; B — 15 kA; C — 16 kA; D — 17 kA

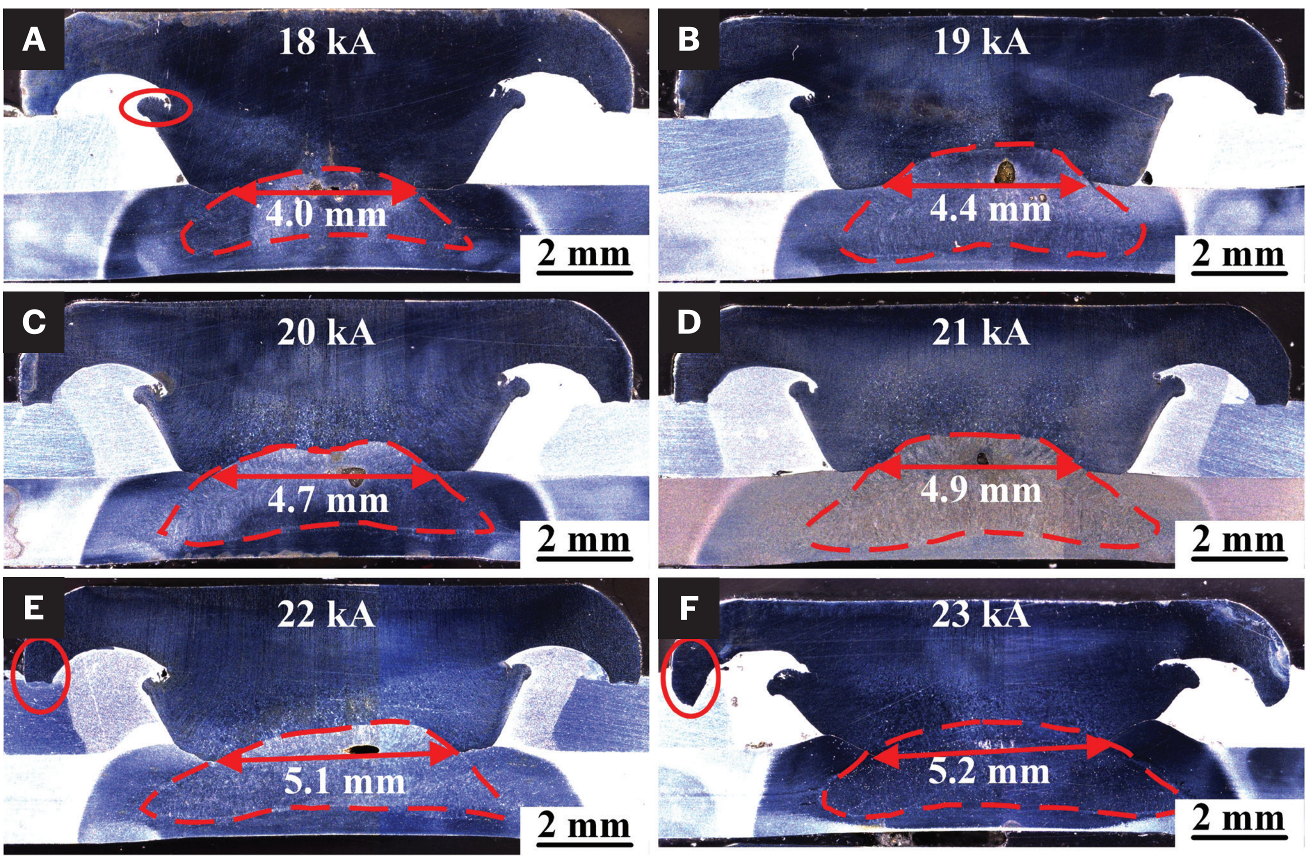

Fig. 5 — Macroscopic morphologies of joints made with different welding currents: A — 18 kA; B — 19 kA; C — 20 kA; D — 21 kA; E — 22 kA; F — 23 kA (piercing stage: 6000 N-16 kA-40 ms, welding stage: 6000 N-100 ms).

process consisted of the positioning stage, piercing stage, cooling stage, welding stage, and holding stage, as shown in Fig. 3. During the piercing stage, the rivet pierced the Al sheet until it reached the steel sheet. Meanwhile, some Al was squeezed into the space under the rivet cap, as shown in Fig. 3A. During the welding stage, the contact surface between the rivet leg and the steel sheet was the main heat-generating interface, and a weld nugget formed at this location. In this study, the piercing time was 40 ms, the cooling time was 20 ms, the welding time was 100 ms, and the holding time was 300 ms. The piercing current and the welding current varied from 14~23 kA. The electrode force was 6000 N during welding.

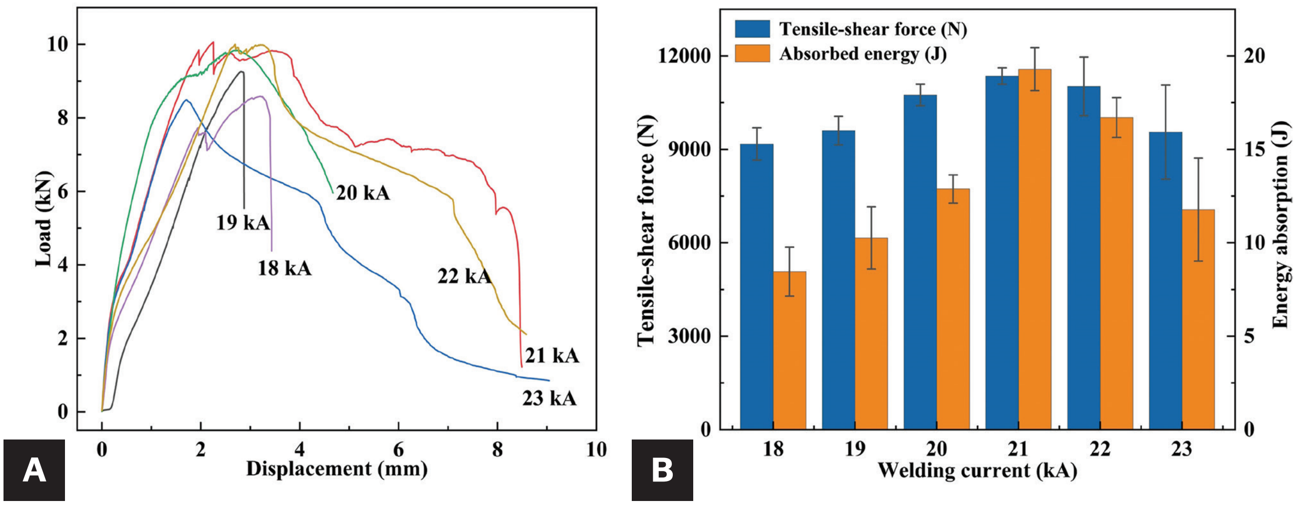

Fig. 6 — Joints' mechanical properties: A — Load-displacement curves; B — average maximum tensile-shear force and absorbed energy.

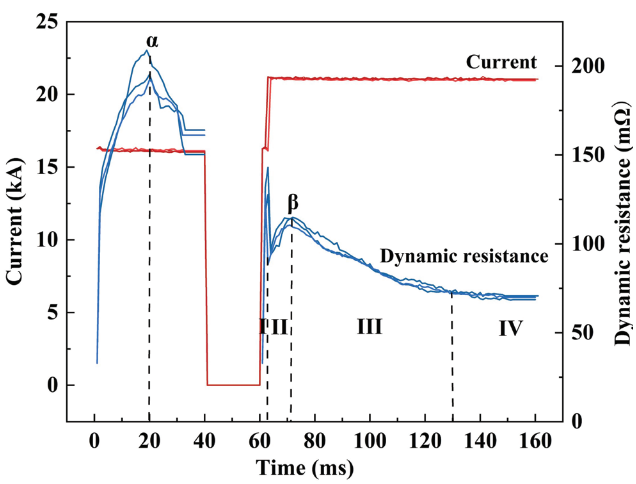

Fig. 7 — Current and dynamic resistance curves of the RRW process under optimal parameters (piercing stage: 16 kA-40 ms, welding stage: 21 kA-100 ms).

Analysis Methods

After welding, the RRWed joints were cut out from the nugget center using electrical discharge machining equipment. The samples were sectioned, cold mounted, and prepared using standard metallographic methods through 2000-grit grinding paper. Afterward, samples were polished with 1.0 µm diamond polishing agent then etched by Keller solution (1% HF, 1.5% HCl, 2.5% HNO_3, and 95% H_2O) for 10 s and 4% nitric acid alcohol for 2 s at room temperature. The macroscopic morphologies of the joints were observed using a super-depth-of-field ZEISS Smartzoom 5 microscope. The samples' microstructure, element segregation, and fracture morphology were analyzed by scanning electron microscopy (SEM, Quanta FEG 250). To determine the chemical compositions in the weld nugget, energy-dispersion X-ray spectroscopy (EDS) analyses were conducted. The microhardness of the welded joints was measured by a Wilson VH1102 microhardness tester with a loading force of 500 g, dwell time of 15 s, and interval of 0.2 mm. Quasi-static tensile-shear tests were performed on a TSE105D universal testing machine (100 kN) with a constant tensile rate of 2 mm/min at room temperature. Three replicas were made for each joint condition. Black-and-white dot patterns were applied as pretreatment for the digital image correlation (DIC) test to observe the strain behavior during the tensile-shear test. The results were analyzed using VIC-2D software.

Results

Determining the Optimal Parameters

Piercing Stage

Figure 4 shows the macromorphologies of joints made with different piercing currents. During the piercing stage, the rivet leg gradually pierced the Al sheet under the effects of resistance heat and electrode force, resulting in significant lateral upset of the rivet leg. Meanwhile, some Al was extruded into space under the rivet cap (see the red circle in Fig. 4A). Detailed microstructure analysis indicated that the Al sheet was melted during the piercing stage, which will be shown in the section "Microstructure of the Pierced Joint." As the piercing current increased from 14 kA to 16 kA, the contact diameter between the rivet leg and the steel sheet expanded from 3.9 mm to 4.6 mm, as shown in Figs. 4A–C. Some melting of the Al was observed at the contact between the left edge of the rivet cap and the Al, as shown in Fig. 4C. When the piercing current further increased from 16 kA to 17 kA, the contact diameter showed little change and a noticeable gap appeared at the contact area between the rivet leg and the Al sheet (see the red circle marked in Fig. 4D). Large pores were also evident in the Al that was

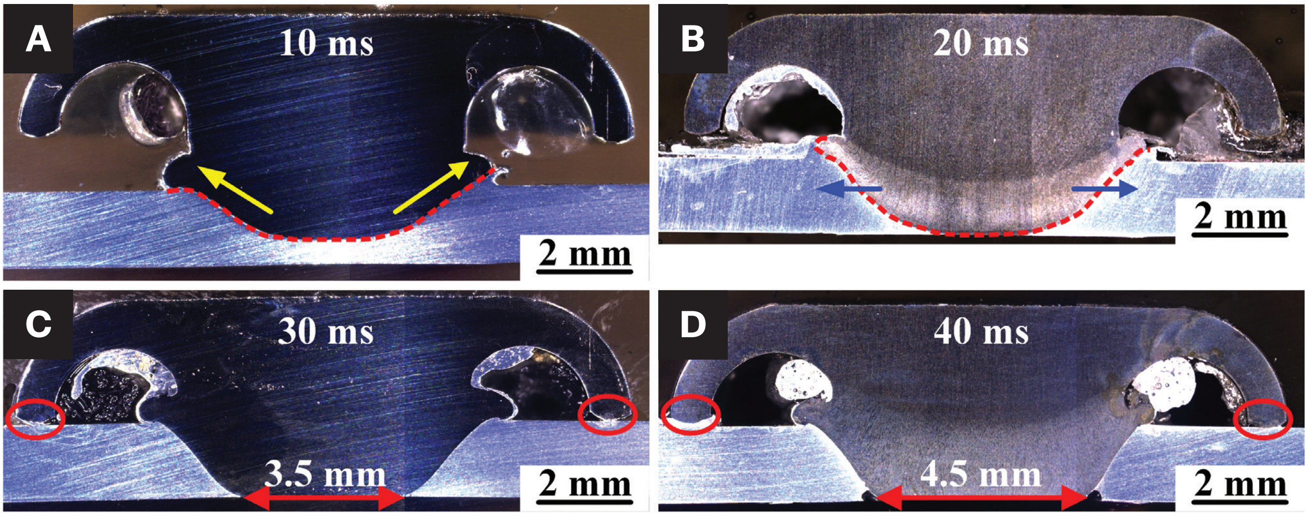

Fig. 8 — Macroscopic morphologies of the RRW joints under different piercing times: A — 10 ms; B — 20 ms; C — 30 ms; D — 40 ms (piercing stage: 6000 N-16 kA).

squeezed into the rivet cap (Fig. 4D). These observations indicated that the piercing current was excessive. Therefore, 16 kA was selected as the optimal piercing current for subsequent research.

Welding Stage

Figure 5 shows the macroscopic morphologies of the joints made with different welding currents. By comparing each image in Fig. 5 with Fig. 4C, it can be seen that the space under the rivet cap was completely filled with Al after welding. Microstructure analysis (see "Microstructure and Joint Properties") showed that the additional Al was squeezed into the rivet cap in its molten state. With the increasing welding current, the nugget diameter at the interface increased from 4.0 mm to 5.2 mm. When the welding current exceeded 21 kA, there was obvious spatter during the welding process. Especially when the welding current was 23 kA, the edge of the rivet cap was pressed into the Al sheet, as marked in the Fig. 5F (red circle), leading to the significantly reduced mechanical property of the joint.

To further explore the optimal welding parameters, the joints' tensile-shear properties are presented in Fig. 6. Figure 6A shows the typical load-displacement curves and Fig. 6B shows the average maximum tensile-shear force and the absorbed energy of the joints made with different welding currents. With increasing welding current, the average tensile-shear force and the absorbed energy of the joints first increased first then decreased. When the welding current was below 21 kA, with the increase of welding current, the increase in heat input made the nugget diameter increase, which improved the joint-bearing capacity. When the welding current was 21 kA, the average tensile-shear force and the absorbed energy of the joints reached the maximum, which was 11.4 kN and 19.3 J, respectively. With the further increase of welding current, the average tensile-shear force and the absorbed energy of the joints decreased. This was likely due to higher welding currents leading to the formation of more IMCs and an increased risk of spatter generation. Finally, 21 kA was selected as the optimal welding parameter for subsequent research.

Dynamic Resistance

Figure 7 shows plots of current and dynamic resistance versus time for three samples produced under optimal parameters. During the piercing stage, the current rapidly increased to 16 kA and remained constant. The dynamic resistance first increased, reached the α peak at 20 ms, and then decreased. This was an interesting phenomenon since in conventional resistance spot welding, dynamic resistance shows a downward trend at the beginning (Refs. 28–30). This phenomenon will be discussed with the microstructure and microhardness results in the "Discussion" section. Figure 8 shows the macroscopic morphologies of the joints at different piercing times. As shown in Fig. 8B, the rivet leg had just pierced the Al sheet and made contact with the steel sheet at 20 ms. Consequently, the piercing stage could be divided into two phases: the rivet leg piercing the Al sheet and the rivet leg expanding at the contact surface.

During the first phase of piercing, the rivet leg underwent significant lateral upsetting and exhibited a taper shape at its bottom, as shown by the yellow arrow in Fig. 8A. The taper bottom of the rivet leg gradually pierced the Al sheet and made contact with the steel sheet, with the piercing time being 20 ms, as shown in Fig. 8B. In the second phase of piercing, the rivet leg was mainly upset deformed.

During the welding stage, the current rapidly increased to 21 kA and then remained constant. The dynamic resistance first decreased (phase I), then increased, reached the β peak at about 70 ms (phase II), then decreased again (phase III), and finally tended to be stable (phase IV). To further investigate the reasons behind the changes in dynamic resistance during the welding stage, Fig. 9 shows the macroscopic morphologies of the joints at different welding times. Figure 9A shows joint marcomorphology in phase I and II. Compared with Fig. 8D, the joint began to be upset in the

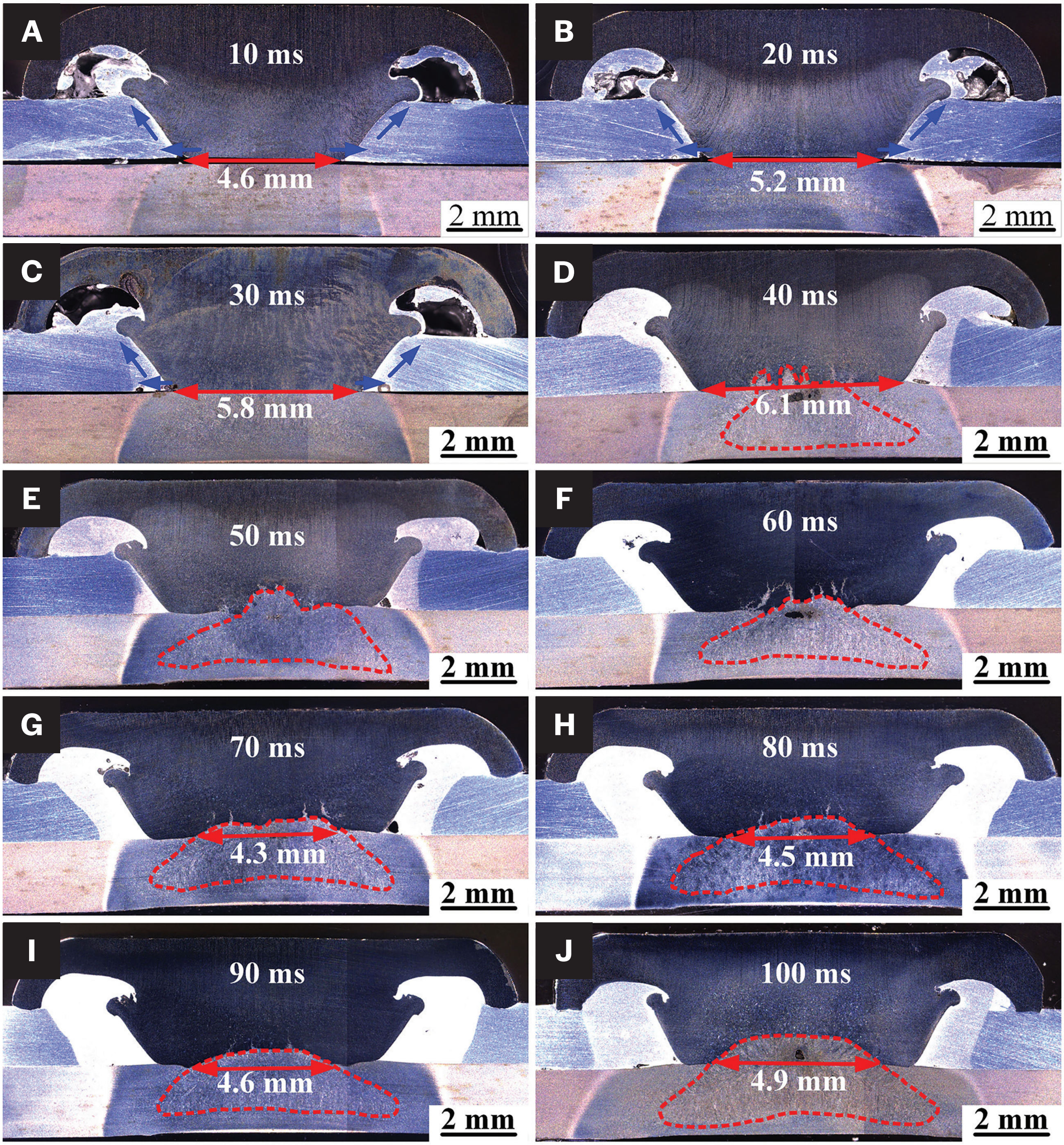

Fig. 9 — Macroscopic morphologies of the RRW joints under different welding times: A — 10 ms; B — 20 ms; C — 30 ms; D — 40 ms; E — 50 ms; F — 60 ms; G — 70 ms; H — 80 ms; I — 90 ms; J — 100 ms (piercing stage: 6000 N-16 kA-40 ms, welding stage: 6000 N-21 kA).

welding stage. Figures 9B–F show the macromorphologies of joints in phase III. The rivet leg continued to be upset, and the Al on the side wall of the rivet leg was squeezed into the rivet cap. At a welding time of 40 ms, the rivet cap was filled by Al, and a weld nugget formed inside the steel sheet rather than at the interface, as shown in Fig. 9D. Afterward, the weld nugget gradually grew toward the rivet. Phase IV was the last 40 ms of welding, and the dynamic resistance remained almost constant. Figures 9G–J show the nugget profiles in this phase. The nugget grew gradually, with a similar profile during phase IV.

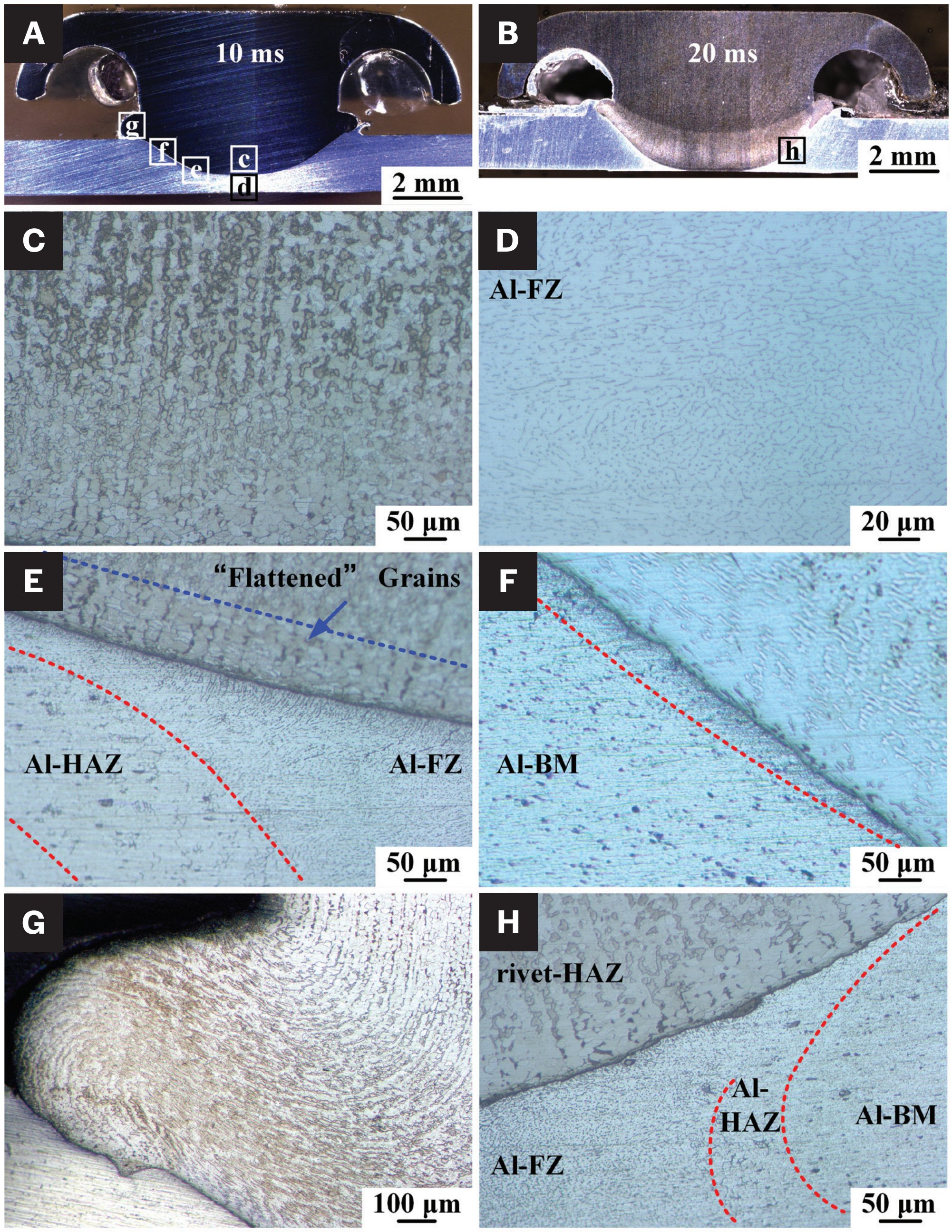

Fig. 10 — Macro- and microstructures of pierced joints: A — Macrostructure of the pierced joint with piercing time of 10 ms; B — macrostructure of the pierced joint with piercing time of 20 ms; C — microstructure of the rivet near the Al/rivet interface; D — microstructure of the Al sheet just under the rivet; E and F — microstructure at the Al/rivet interface; G — microstructure in the fold area of the rivet; H — microstructure at the Al/rivet interface with piercing time of 20 ms.

Microstructure and Joint Properties

Microstructure of the Pierced Joint

Figure 10 shows the microstructures of the pierced joints when the piercing time was 10 ms and 20 ms. The microstructures of the rivet near the Al/rivet interface were ferrite and pearlite (rivet-HAZ), which were the same as the microstructures of the rivet base material, as shown in Fig. 10C. This observation indicated that the rivet did not melt during the early stage of piercing. In addition, a layer of fine grains close to the Al/rivet interface could be observed. The microstructure of the Al sheet just under the rivet was the typical solidification structure of aluminum alloy, as shown in Fig. 10D. Moving upward along the Al/rivet interface, the amount of melted Al (Al-FZ) became smaller, and almost no melted Al was observed in Fig. 10F. A layer of "flattened" grains could be observed in the rivet near the Al/rivet interface, as shown in Figs. 10E and F. Evidence for plastic flow could be

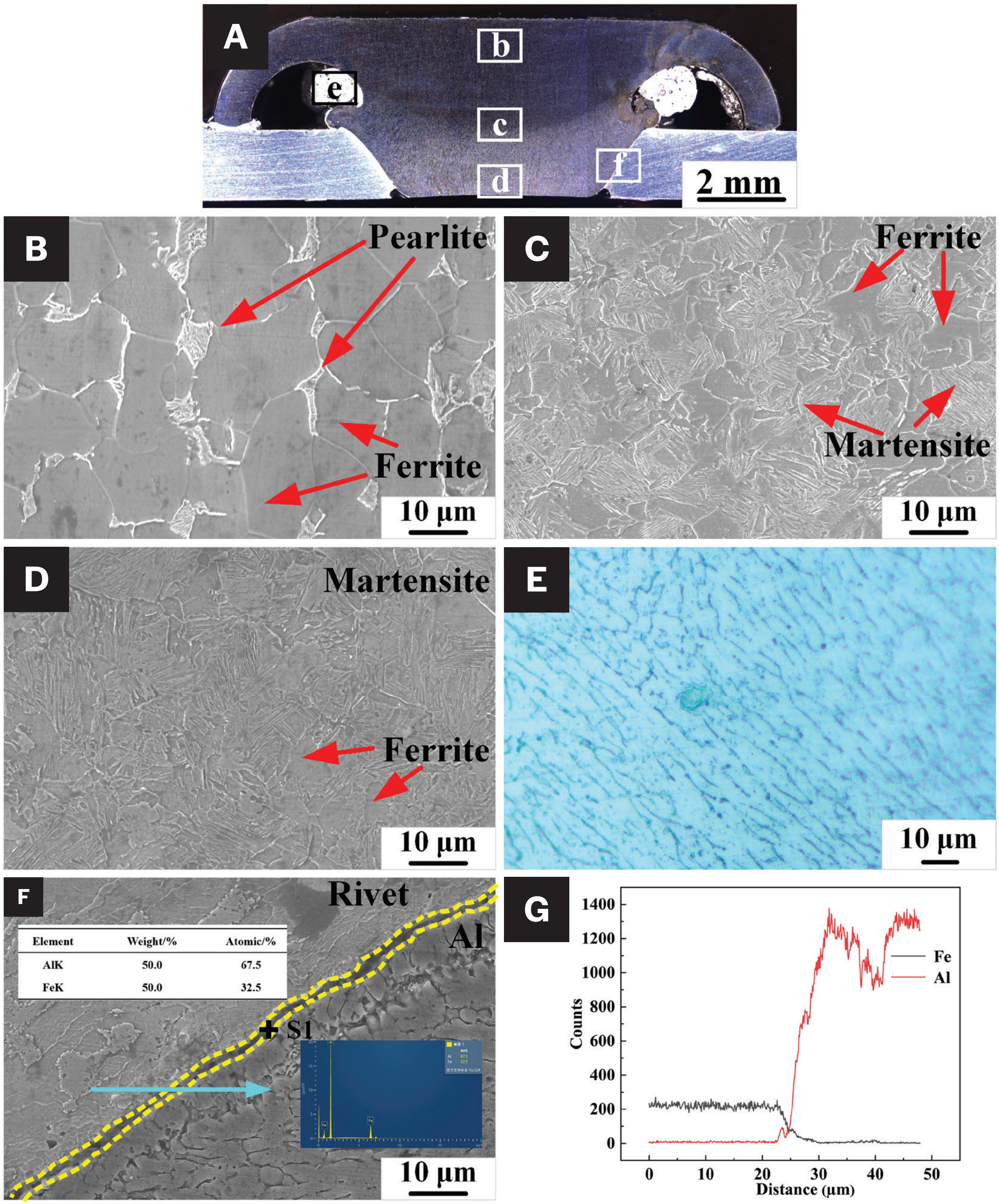

Fig. 11 — Macro- and microstructure of the pierced joint with piercing time of 40 ms: A — Macrostructure of the pierced joint; B — microstructure in the upper region of the rivet; C — microstructure in the middle area of the rivet; D — microstructure in the bottom area of the rivet; E — microstructure of the extruded Al; F — microstructure in the Al/rivet interface; G — line scan result of the Al/rivet interface.

observed in the fold area of the rivet, as shown in Fig. 10G. Figure 10H shows the microstructure at the Al/rivet interface with a piercing time of 20 ms. The results were similar to the joint made with a piercing time of 10 ms.

Figure 11 shows the macromorphology and microstructures of the pierced joint with a piercing time of 40 ms. After the piercing process was completed, the microstructure in the upper region of the rivet was comprised of ferrite and pearlite, which was consistent with those of the BM, as shown in Fig. 11B. The microstructure in the middle region of the rivet mainly consisted of ferrite and fine martensite, as shown in Fig. 11C. The bottom region of the rivet was characterized by martensite and fine ferrite, as shown in Fig. 11D. Some Al was extruded into the space under the rivet cap. The microstructure of this part of the Al was typical solidification microstructure of Al alloy, as shown in Fig. 11E. A uniform IMCs layer could be observed at the Al/rivet, as marked by the yellow dashed line in Fig. 11F. There was little difference in the IMC layers' size and the composition profiles at the various locations on the Al/rivet interface of the pierced joint. Therefore, this paper only presents the EDS result in one point (S1). The atomic ratio of Al to Fe was about 7:3.

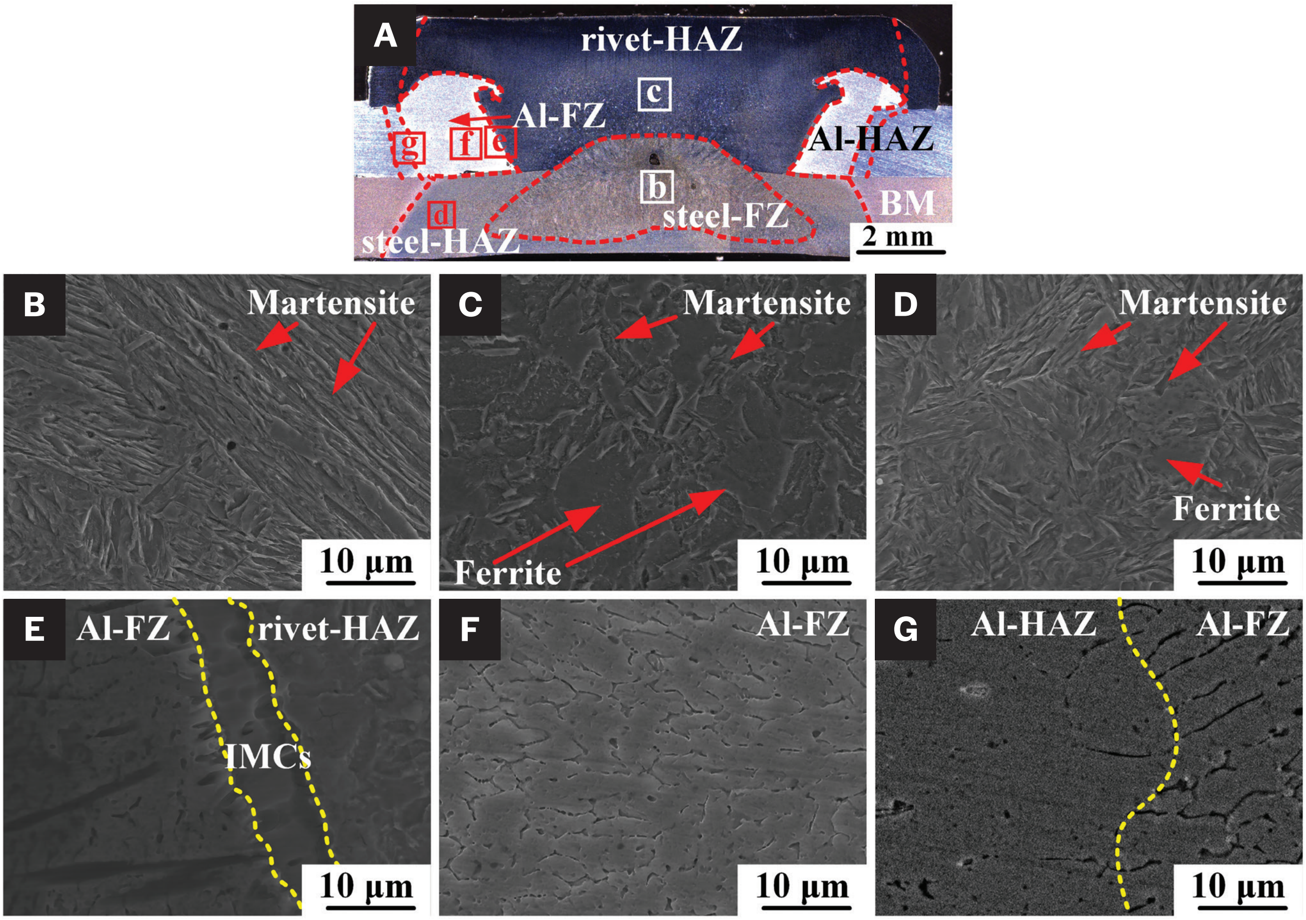

Fig. 12 — Macro- and microstructure of the welded joint: A — Macrostructure of the joint; B — rivet HAZ; C — steel FZ; D — steel HAZ; E — Al/rivet interface; F — Al FZ; G — Al HAZ.

Microstructure of the Welded Joint

Figure 12 shows the macrostructure of the welded joint and each region under the optimal parameters. The joint can be divided into steel sheet fusion zone (steel-FZ), rivet heat affected zone (rivet-HAZ), steel sheet heat affected zone (steel-HAZ), Al sheet fusion zone (Al-FZ), Al sheet heat affected zone (Al-HAZ) and base metal (BM), as shown in Fig. 12A.

The steel-FZ exhibited a mushroom shape, with the rivet side convex and the steel sheet side concave. The microstructure of the steel-FZ was characterized by coarse lath martensite, as shown in Fig. 12B. The microstructures of the rivet-HAZ and the steel-HAZ were characterized by lath martensite and ferrite, as shown in Figs. 12C and D. The microstructure at the joint between the rivet and the Al sheet is shown in Fig. 12E. A uniform IMCs layer existed between the rivet-HAZ and the Al-FZ. The microstructure of the Al-FZ was consistent with the solidification structure of the Al alloy, as shown in Fig. 12F. In the Al-HAZ, the unfused base material was subjected to the welding thermal cycle, leading to the dissolution and precipitation of the secondary phase. Coarse, irregular dendrites also appeared, as shown in Fig. 12G.

Figure 13 shows the SEM and EDS analysis results of the interface between the rivet leg and the Al sheet for the optimized parameters. The line scan results indicated the formation of approximately 4.7-μm thick Fe-Al IMCs between the Al sheet and the rivet leg (Fig. 13B). To further investigate the composition of the IMCs at the interface, three points at the interface were selected for elemental composition analysis. The results were consistent and showed that they contained 70% Fe and 30% Al, as shown in Fig. 13C.

Microhardness Distribution

Figure 14A depicts the microhardness distribution of a pierced joint. For the rivet, the microhardness of the BM was about 130 HV, and the microhardness gradually increased from the top to the bottom of the rivet (Line A). Along the bottom of the rivet leg to the edge of the rivet leg, the microhardness of the rivet gradually increased from 220 to 300 HV (Line B). The microhardness of the Al sheet gradually increased upward along the Al/rivet interface.

Figures 14B and C show the hardness distribution of the welded joints made with three welding currents. It can be seen that the change trends of the microhardness under the three welding currents were the same. In the vertical direction, the microhardness of the rivet-HAZ, steel-FZ, and steel-HAZ increased continuously. In the horizontal direction, the microhardness of the rivet-HAZ, Al-FZ, Al-HAZ, and

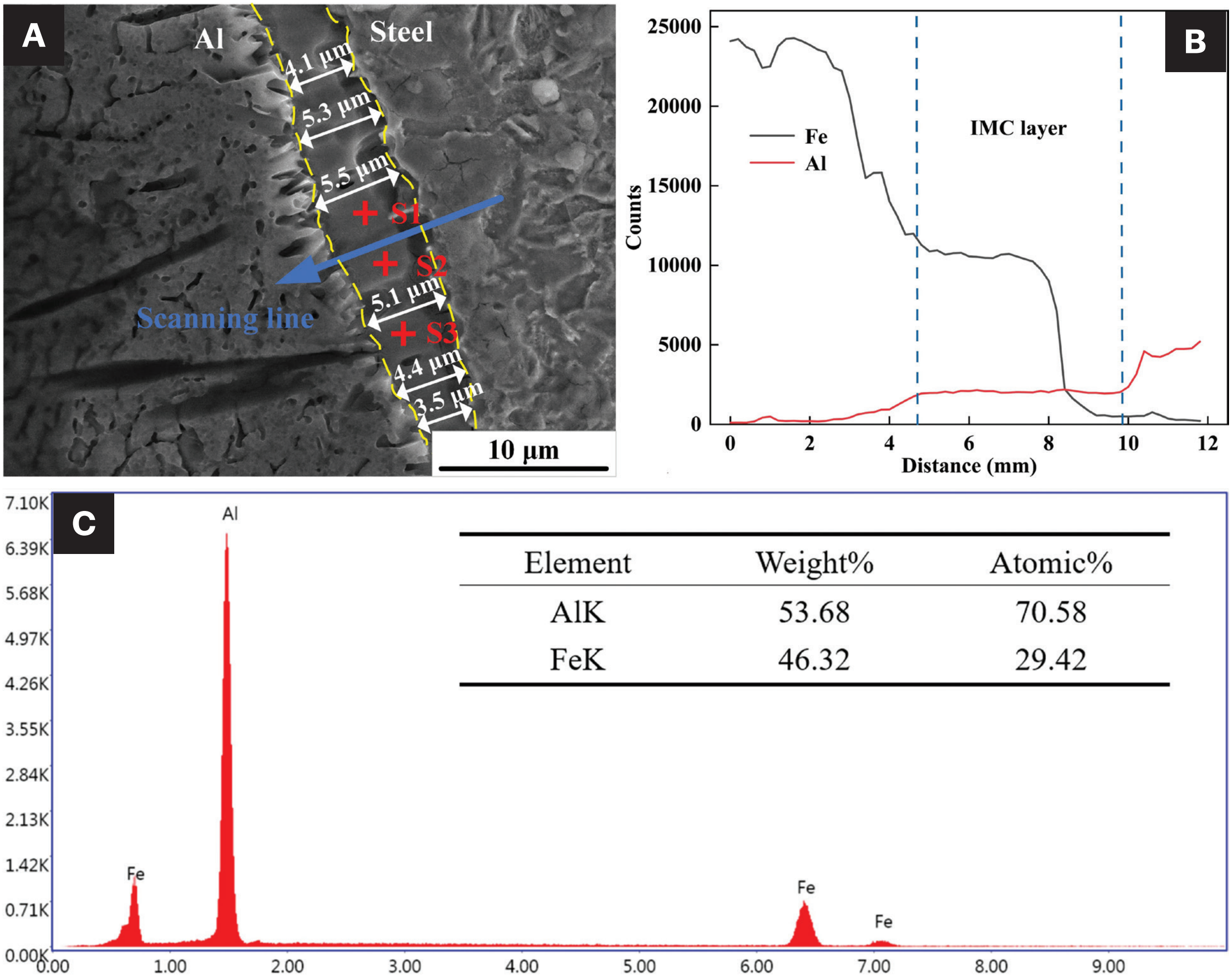

Fig. 13 — EDS analysis of the Al-Fe IMC layer: A — High magnification of SEM image; B — EDS line scan result; C — EDS result of point S2.

Al-BM showed a trend of decreasing first and then increasing. In addition, the higher the welding current, the harder the microhardness in the rivet-HAZ, steel-FZ, and steel-HAZ (Fig. 14B). The microhardness in the steel-FZ of the joint welded with a current of 19 kA was approximately 500 HV. In comparison, it reached 700 HV for the joint welded with a current of 23 kA.

Failure Modes

Three failure modes were observed in the tensile-shear tests, namely interface failure (IF), pull-out failure (PF), and Al sheet failure (AlF), as shown in Fig. 15. When the welding current was less than 19 kA, the nugget diameter was small, and the failure mode of the joint was IF. The failure occurred at the contact interface between the rivet leg and the steel sheet, as shown in Fig. 15A. When the welding current was 20 kA or 21 kA, the nugget diameter was large, and the joints experienced PF. The failure occurred at the steel sheet side, and the steel nugget was pulled out from the steel sheet, as shown in Fig. 15B. When the welding current was higher than 22 kA, the failure mode of the joint was AlF, as shown in Fig. 15C. Figure 16 shows the cross-section of the joint fractured through AlF. Although multiple cracks can be observed in the joint, the joint ultimately fractured along the Al/rivet interface.

Figures 17A–C illustrate the strain distribution in joints exhibiting IF, PF, and AlF using DIC, respectively, and Fig. 17D shows the corresponding load-displacement curves in the three types of joints. Before reaching the peak load, the strain near the rivet cap increased with the applied load. At the peak load, the strain in this region reached its maximum.

Figure 18 shows the SEM images of the fracture surfaces of different failure modes. Figure 18A shows the SEM image of the Al sheet side under the IF mode, characterized primarily by tear ridges. Figure 18B shows the SEM image of the rivet leg side under the PF mode, revealing both smooth tear ridge structures and fine dimple structures. Figure 18C shows the SEM image of the Al sheet fracture under the AlF mode, exhibiting fine dimple structures.

Discussion

Nugget Formation Process

Based on the experimental results, the nugget formation process of RRW is summarized in Fig. 19. Figure 19A shows the starting position. Figures 19B and C show the first phase of the piercing stage. Under the piercing current, the Al sheet directly below the rivet melted while the Al sheet under the edge of the rivet leg still kept a solid state (which is supported by Figs. 10D–F). The microhardness of the Al sheet along the Al/rivet interface (Line C in Fig. 14A) also verified the above statement. At this time, the rivet began to press into the Al sheet under the action of the piercing force. The molten Al was squeezed into space under the rivet cap. The rivet leg was subject to greater resistance in its edge area, resulting in plastic flow (see Fig. 10G), which is macroscopically upsetting. Work hardening was also observed in this area (Line B in Fig. 14A). The plastic deformation and work hardening experienced by the rivet leg may have contributed to the increase of dynamic resistance in the first phase of the piercing stage (Fig. 7), which could have been due to the increased numbers of electron-scattering dislocations (Ref. 31).

Figure 19D shows the second phase of the piercing stage. In this phase, the contact area between the rivet and the steel sheet gradually expanded. In addition, the contact of the rivet cap edge with the Al sheet created a new path for shunting the welding current (see the red circle marked in Fig. 19D). The above two observations were likely to have contributed to the reduction of dynamic resistance in the second phase of piercing stage (Fig. 7). The Al in contact with the rivet leg did not all melt at the same time but increased as the piercing time increasing. When the piercing was completed, the Al in contact with the rivet legs melted, as evidenced by the presence of IMCs at the Al/rivet interface, as shown in Fig. 11.

Figures 19E–G show the welding stage in RRW. During the welding stage, the joining occurred between the steel rivet and the steel sheet, and, therefore, the welding behavior at this time was similar to the traditional RSW of steel. This stage can be divided into four phases based on the dynamic resistance curve, as mentioned in the section "Dynamic Resistance." In phase I, the dynamic resistance decreased due to the surface breakdown and the asperity softening. Since the bottom surface of the rivet leg and the top surface of the steel sheet were already broken down to a certain degree during the piercing stage, phase I lasted only 1~2 ms. In phase II, as the temperature increased, the bulk resistance increased, increasing dynamic resistance. The dynamic

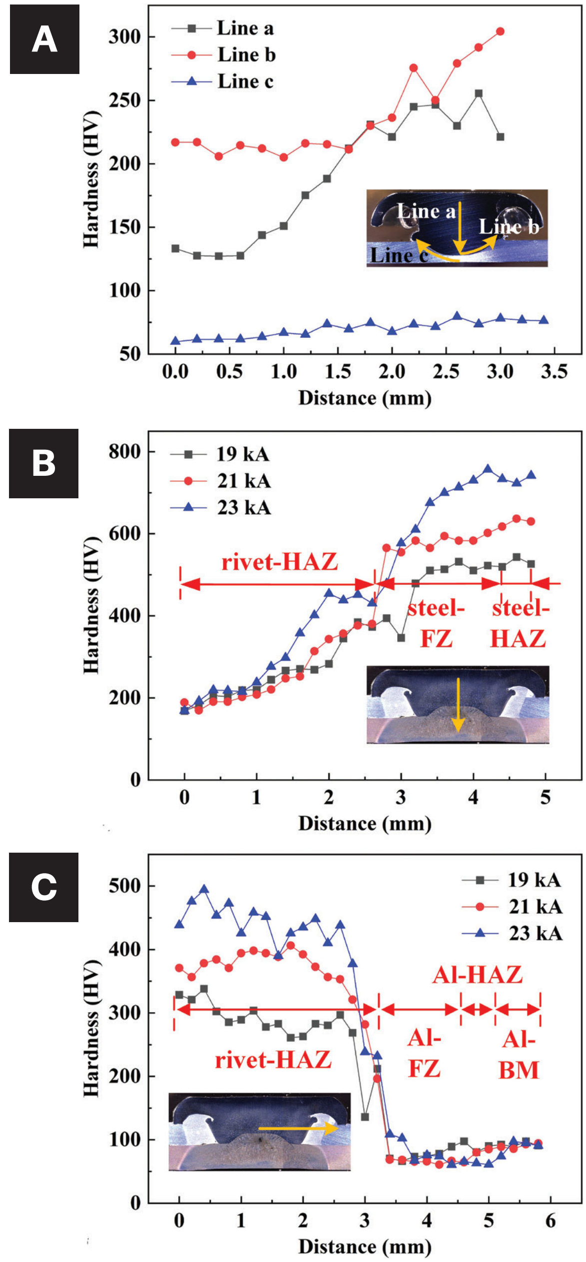

Fig. 14 — Microhardness distribution of: A — The pierced joint with a piercing time of 10 ms; B — joints made with different welding parameters (vertical direction); C — joints made with different welding parameters (horizontal direction).

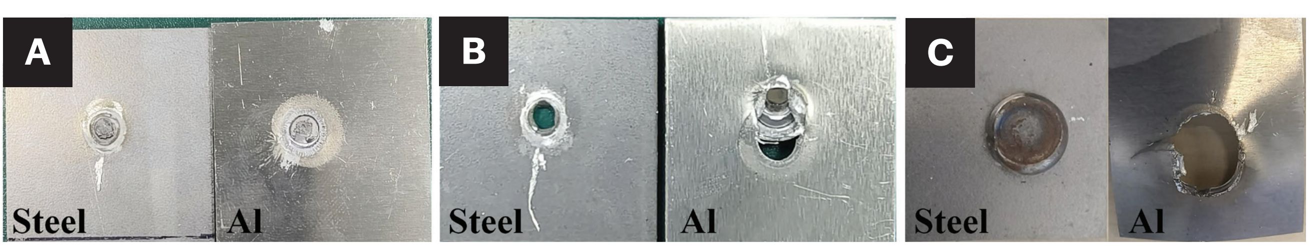

Fig. 15 — Three failure modes of the joints: A — Interface failure; B — pull-out failure; C — Al sheet failure.

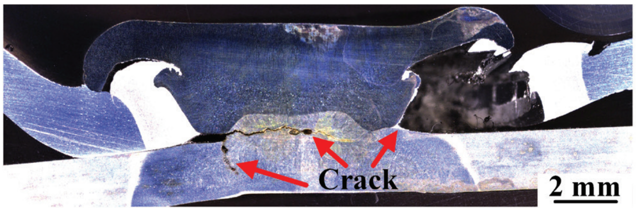

Fig. 16 — The cross section of the joint fractured through the AlF.

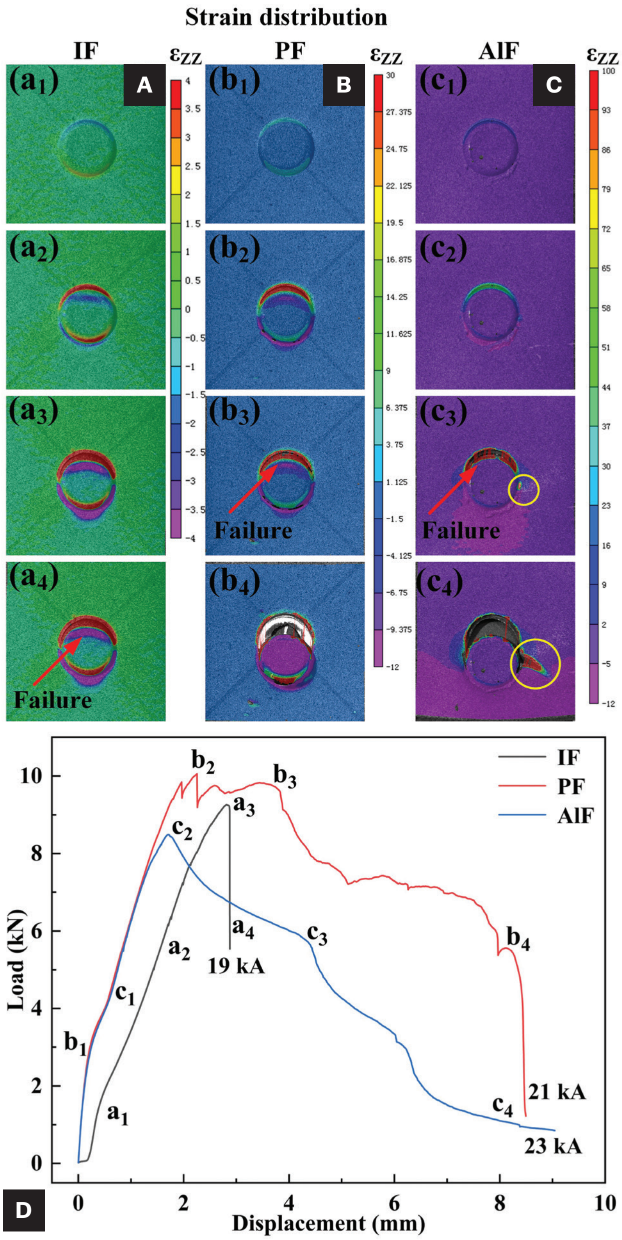

Fig. 17 — Von Mises equivalent strain field of the joints during the tensile-shear test: A — IF; B — PF; C — AlF; D — the corresponding load-displacement curves during the tensile-shear test.

resistance increased to its β peak at a welding time of about 10 ms. Xia et al. (Ref. 32) pointed out that at this time, the temperature in the joint is close to Ac_3. No weld nugget was formed at this time. Phase III lasted from the welding time of 10 ms to 60 ms. In this phase, although the bulk resistance increased with the increase in temperature, the increased contact diameter between the electrode/rivet interface and between the rivet leg/steel sheet interface led to the overall reduction of dynamic resistance (Ref. 33). A weld nugget was initially formed inside the steel sheet rather than at the interface, as shown in Fig. 19F. This result likely stemmed from the higher resistivity of the steel sheet and greater thermal conductivity of the Al sheet that dissipated heat from the rivet. Phase IV involved the last 30 ms of welding time. During this phase, the weld nugget grew slowly, and the dynamic resistance remained almost constant. This observation indicated that the welding process was stable.

Microstructure Transformation

At the beginning of the piercing stage, the rivet pierced into the Al sheet in its solid state, and the rivet leg temperature should not have exceeded Ac_3. After the piercing finished, the peak temperature of the rivet leg exceeded Ac_3 but was below its melting point, resulting in extensive austenitization. The Fe-Al IMCs were produced after the piercing stage was finished.

During the welding process, the grains in the fusion zone were likely solidified to form high-temperature ferrite and then transformed into austenite. Due to the rapid cooling rate, the austenite transformed into coarse lath martensite. For the rivet-HAZ and the steel-HAZ, the peak temperatures exceeded Ac_1 but remained below Ac_3 based on microstructural observations, resulting in the transformation of the microstructure into ferrite and austenite. Upon rapid cooling, the austenite subsequently transformed into martensite, while the ferrite remained unchanged. Consequently, the final microstructure consisted of martensite and ferrite. For the Al-FZ, the grains were influenced by their bulk resistance heating and the heat transfer from the rivet leg, causing the temperature to rise rapidly beyond its melting point and forming the solidification structures. It was inferred from the EDS spectra results that the IMC between the rivet leg and the Al sheet was mainly Fe_2Al_5.

The microhardness results demonstrated that higher welding currents produced greater hardness in the rivet and steel sheet. This was primarily due to the formation of coarser martensite in the FZ at higher welding currents. However, in the Al sheet, higher welding currents enlarged the area of the Al FZ and the HAZ, both exhibiting a hardness of around 60 HV, indicating a softening region. An excessively large softening region reduced the mechanical performance of the joint.

Failure Analysis

The joint with IF fractured along the interface between the Al sheet and the steel sheet after reaching the peak load, as shown in Fig. 17A, location 4. For the joint with PF, the joint did not completely fracture at the peak load. Instead, the fracture occurred at the junction between the rivet leg

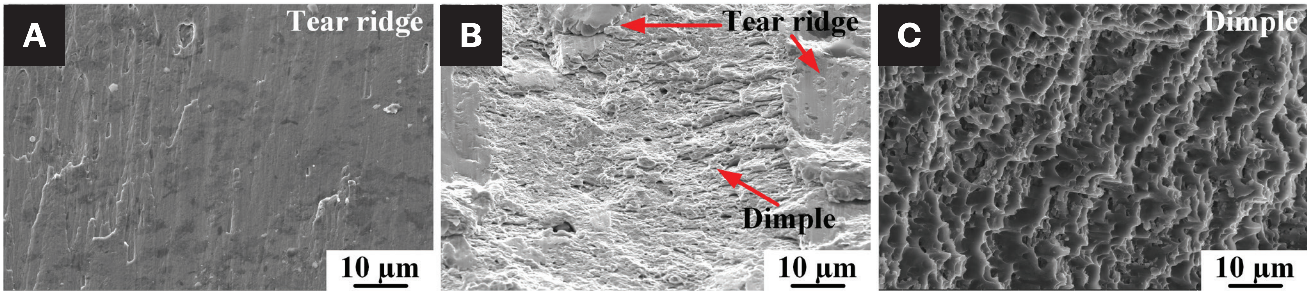

Fig. 18 — SEM photos of joints fractured through: A — Interface failure; B — pull-out failure; C — Al sheet failure.

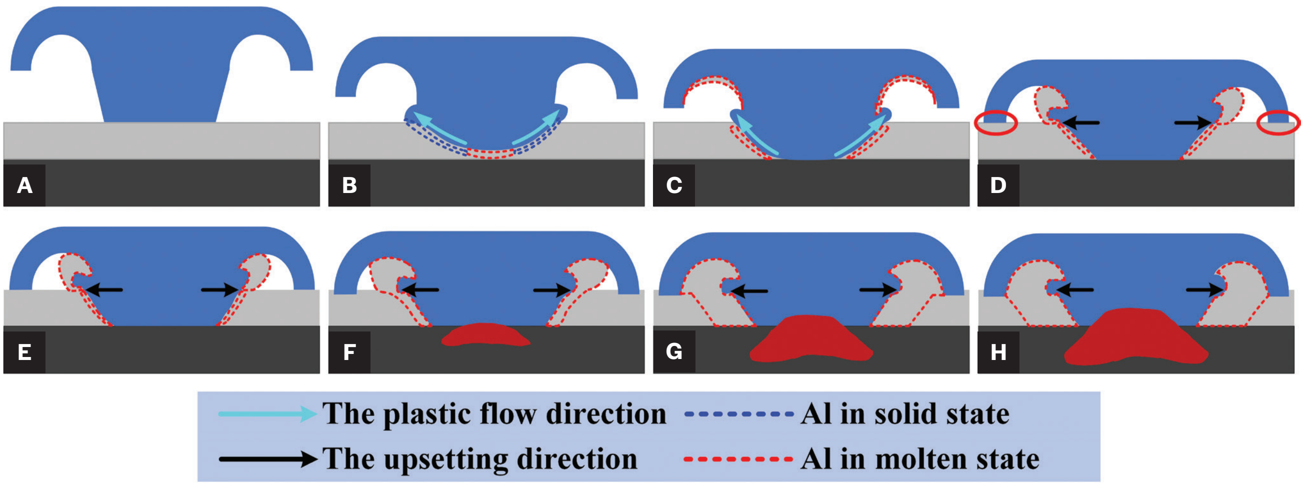

Fig. 19 — Schematic diagram of the nugget formation process: A — Positioning stage; B–D — piercing stage; E–H — welding stage.

and the Al sheet, resulting in a sudden load drop at point b_2 in Fig. 17. With further load increase, strain remained concentrated at the fracture site between the rivet and the Al sheet. Subsequently, the joint gradually fractured along the outer edge of the FZ on the steel sheet side, eventually penetrating the steel sheet and leading to a pull-out fracture, as depicted in Fig. 17B, location 4. For the joint with AlF, the initial fracture occurred at the junction between the rivet leg and the Al sheet after reaching the peak load. As the load continued to increase, strain concentration appeared at the edge of the fractured Al sheet, as indicated by the yellow circle in Fig. 17C, location 3. Under the applied load, a crack formed at these strain concentration points in the Al sheet, propagated through the Al sheet, and ultimately resulted in Al sheet fracture.

The IF mode displayed a typical brittle fracture. The PF mode showed a ductile-brittle mixed fracture. This mixed mode suggested that the joint toughness in the PF mode was superior to that in the IF mode. Although the fracture surface of the AlF mode showed characteristics of ductile fracture, the shear-tensile force of the joints fractured through AlF mode was not optimal. Multiple cracks can be observed in the joint cross-section after AlF mode (Fig. 16), demonstrating competition in the crack propagation process before joint failure.

Conclusions

In this study, AA6016-T6 Al alloy and CR1180T UHSS were joined by RRW with solid rivets. The nugget formation process, microstructure, and joint mechanical properties were investigated. The main conclusions are summarized as follows.

1. Piercing occurred when the Al directly below the rivet leg melted, but the Al under the edge of the rivet leg was not completely melted. The edge of the rivet leg underwent plastic deformation and flow under the action of partially melted Al, which manifested macroscopically as upsetting. Al was extruded into the space under the rivet cap when in a liquid state. The IMCs at the Al/rivet interface began to form during the piercing stage. The liquid nugget was first formed inside the steel sheet and gradually grew toward the rivet, eventually forming a mushroom-shaped weld nugget.

2. The joining mechanism in RRW with solid rivets included a steel nugget at the main load-bearing interface and a layer of Fe-Al IMC (~4.7 μm) along the Al/rivet interface. Under the optimal parameters of electrode force 6000 N, piercing stage 16 kA-40 ms, and welding stage 21 kA-100 ms, the maximum average tensile-shear force of the joints reached 11.4 kN, which is the highest among existing research, demonstrating the potential application prospect of this technology.

3. Three failure modes were identified: brittle interface failure, ductile-brittle mixed pull-out failure, and ductile Al sheet failure. Under the optimal parameters, the failure mode of the joint was a pull-out failure. The simultaneous presence of multiple crack sources led to a decrease in the tensile-shear load of joints experiencing Al sheet failure.

Data Availability

The raw/processed data required to reproduce these findings cannot be shared as the data also forms part of an ongoing study.

Declaration of Competing Interest

The authors declare no competing interest.

Acknowledgement

This research was funded by the National Natural Science Foundation of China (No. 52375372) and the Science and Technology Planning Project of Tianjin (No.22YFFCYS00090).

References

1. Sakundarini, N., Taha, Z., Abdul-Rashid, S. H., and Ghazila, R. A. R. 2013. Optimal multi-material selection for lightweight design of automotive body assembly incorporating recyclability. *Materials & Design* 50: 846–857.

2. Zhang, W., and Xu, J. 2022. Advanced lightweight materials for Automobiles: A review. *Materials & Design* 221: 110994.

3. Xue, Z. G., Yang, Z., Xu, C. C., Chen, Z. M., Wang, Z. H., Zhou, Q. Y., Liu, J. P., and Li, L. X. 2023. An improved simplified model of self-piercing riveted joints for predicting quasi-static mechanical behavior of steel–aluminum hybrid components. *Journal of Manufacturing Processes* 108: 457–474.

4. Duan, L. B., Du, Z. P., Ma, H. F., Li, W., Xu, W., and Liu, X. 2023. Simplified modelling of self-piercing riveted joints and application in crashworthiness analysis for steel-aluminium hybrid beams. *Journal of Manufacturing Processes* 85: 948–962.

5. Li, M. F., Tao, W., Zhang, J. Z., Wang, Y. J., and Yang, S. L. 2022. Hybrid resistance-laser spot welding of aluminum to steel dissimilar materials: Microstructure and mechanical properties. *Materials & Design* 221: 111022.

6. Queval, J., Geslain, E., Pouvreau, C., Broussaud-Laloue, P., and Loyer., S. 2024. Joining thin galvanized low carbon steel sheet to AA6056-T4 by resistance spot welding and adhesive weld bounding. *Journal of Manufacturing Processes* 110: 70–81.

7. Yang, Y., Li, Y., Bi, J., Liu, H. W., Ao, S. S., and Luo, Z. 2022. Microstructure and mechanical properties of 2195/5A06 dissimilar joints made by resistance spot welding. *Materials Characterization* 191: 112147.

8. Jia, X., Wei, S. T., and Lu, S. P. 2024. Softening mechanism and failure behavior of 9Cr oxide dispersion strengthened steel resistance spot welded joint. *Journal of Manufacturing Processes* 118: 331–340.

9. Pan, B., Sun, H., Shang, S., Banu, M., Wang, P. C., Carlson, B. E., Liu, Z., and Li, J. J. 2022. Understanding formation mechanisms of intermetallic compounds in dissimilar Al/steel joint processed by resistance spot welding. *Journal of Manufacturing Processes* 83: 212–222.

10. Wan, Z. X., Wang, H., Chen, N. N., Wang, M., and Carlson, B. E. 2017. Characterization of intermetallic compound at the interfaces of Al-steel resistance spot welds. *Journal of Materials Processing Technology* 242: 12–23.

11. Chen, N. N., Wang, M., Wang, H., Wan, Z. X., and Carlson, B. E. 2018. Microstructural and mechanical evolution of Al/steel interface with Fe_2Al_5 growth in resistance spot welding of aluminum to steel. *Journal of Manufacturing Processes* 34: 424–434.

12. Meschut, G., Hahn, O., Janzen, V., and Olfermann, T. 2014. Innovative joining technologies for multi-material structures. *Welding in the World*. 58: 65–75.

13. Ling, Z. X., Ling, Y., Luo, Z., Feng, Y. Q., and Wang, Z. M. 2016. Resistance element welding of 6061 aluminum alloy to uncoated 22MnMoB boron steel. *Materials Manufacturing Processes* 31: 2174–2180.

14. Ling, Z. X., Ling, Y., Luo, Z., Ao, S. S., Yin, Z. H., Gu, Y. L., and Chen, Q. 2017. Microstructure and fatigue behavior of resistance element welded dissimilar joints of DP780 dual-phase steel to 6061-T6 aluminum alloy. *International Journal of Advanced Manufacturing Technology* 92: 1923–1931.

15. Yang, Y., Luo, Z., Bi, Y. B., and Zhang, Y. X. 2023. Nano-scale characterization of intermetallic compounds in dissimilar aluminum-steel resistance element welded joints. *Materials Characterization* 204: 113227.

16. Yang, Y., Bi, Y. B., Su, J., and Luo, Z. 2023. Precipitate characteristic and nanoindentation analysis of resistance element welded DP780 steel and 6061 aluminum alloy joint. *Materials Letters* 347: 134571.

17. Yang, Y., Bi, Y. B., Zhang, Y. X., Su, J., and Luo, Z. 2023. Microstructure and mechanical properties of resistance element welded joints for DP780 steel and 6061 aluminum alloy. *Advance Engineering Materials* 25: 2201795.

18. Hou, W., Hu, S. J., and Wang, P. C. Method of joining dissimilar materials. U.S. Patent 7267736B2, filed 18 December, 2003, and issued 11 September, 2007.

19. Niu, S. Z., Ma, Y. W., Lou, M., Zhang, C. Q., and Li, Y. B. 2020. Joint formation mechanism and performance of resistance rivet welding (RRW) for aluminum alloy and press hardened steel. *Journal of Materials Processing Technology* 286: 116830.

20. Niu, S. Z., Lou, M., Chen, Z. X., Wang, Z. L., Ma, Y. W., Hu, S. Q., Lei, H. Y., and Li, Y. B. 2023. Resistance rivet welding of multilayer dissimilar materials. *Journal of Materials Research and Technology*. 27: 6424–6437.

21. Niu, S. Z., Lou, M., Ma, Y. W., Yang, B. X., Shan, H., and Li, Y. B. 2021. Resistance rivet welding of magnesium/steel dissimilar materials. *Materials Letters* 282: 128876.

22. Niu, S. Z., Wang, Z. L., Lou, M., Ma, Y. W., Lei, H. Y., and Li, Y. B. 2023. Resistance rivet welding of aluminum/titanium dissimilar materials. *Journal of Manufacturing Processes* 108: 141–152.

23. Niu, S. Z., Lou, M., Ma, Y. W., and Li, Y. B. 2021. Study on the microstructure and mechanical performance for integrated resistance element welded aluminum alloy/press hardened steel joints. *Materials Science and Engineering: A* 800: 140329.

24. Fei, L. Y., Feng, Z. Y., Jiang, F., Zhang, Y. M., and Zhao, S. D. 2023. Process optimization of robust bonding between DP590 and AA6061 using resistance riveting welding. *Journal of Manufacturing Processes* 104: 273–288.

25. Fei, L. Y., Feng, Z. Y., Li, H., Jiang, F., Zhang, Y. M., and Zhao, S. D. 2023. Effect of a Zn interlayer on the formation mechanism and mechanical performance of AA6061/DP590 steel resistance riveting welding. *Journal of Materials Processing Technology* 322: 118213.

26. Lou, M., Niu, S. Z., Ma, Y. W., Shan, H., Yang, B. X., and Li, Y. B. 2023. The aging characteristics of resistance rivet welded aluminum/steel joints. *Journal of Materials Research and Technology* 26: 3615–3628.

27. Li, M. Y., Yu, S. B., Yang, Y., Gao, Z. L., Tao, S., Ao, S. S., and Li, Y. 2024. Influence of solid rivet dimensions on the joint performance of resistance rivet welded 6061 aluminum alloy to CR1180T ultra-high strength steel. *Journal of Materials Research and Technology* 32: 1916–1927.

28. Zhou, L., Zhang, T. Y., Zhang, Z. D., Lei, Z. L., and Zhu, S. L. 2022. Monitoring of resistance spot welding expulsion based on machine learning. *Science and Technology of Welding and Joining*. 27: 292–300.

29. Hu, J. M., Bi, J., Liu, H. W., Li, Y., Ao, S. S., and Luo, Z. 2022. Prediction of resistance spot welding quality based on BPNN optimized by improved sparrow search algorithm. *Materials* 15: 7323.

30. Zhou, K., Wang, G., Ren, B. K., Yu, W. X., and Ivanov, M. 2023. Process optimization of aluminum/steel resistance spot welding based on dynamic resistance analysis. *Journal of Materials Science* 58: 17908–17929.

31. Omotoyinbo, J. A., Oladele, I. O., and Shokoya, W. 2014. Effect of the degree of plastic deformation on the electrical resistance and thermal conductivity of Al-Mg-Si alloy. *Leonardo Electronic Journal of Practices and Technologies* 24: 37–50.

32. Xia, Y. J., Lv, T. L., Ghassemi-Armaki, H., Li, Y. B., and Carlson, B. E. 2023. Quantitative interpretation of dynamic resistance signal in resistance spot welding. *Welding Journal* 102: 69-s to 87-s.

MINGYANG LI, **RUOYA SHI**, **SANSAN AO**, and **YANG LI** (*liyang86@tju.edu.cn*) are with the School of Materials Science and Engineering, Tianjin University, Tianjin, China. **SHIBAO YU**, **ZHONGLIN GAO**, and **TAO SHI** are with Tianjin 707 Hi-tech Co. Ltd., China. **AO** and **LI** are also with the International Institute for Innovative Design and Intelligent Manufacturing of Tianjin University in Zhejiang, Shaoxing, China.